Validation of the smooth step model by particle-in-cell/Monte Carlo collisions simulations

Validation of the smooth step model
by particle-in-cell/Monte Carlo collisions simulations

Maximilian Klich, Jan Löwer, Sebastian Wilczek,

Thomas Mussenbrock, Ralf Peter Brinkmann

Department of Electrical Engineering and Information Technology

Ruhr University Bochum, D-44780 Bochum, Germany

(Dated: January 19, 2022)

Abstract

Bounded plasmas are characterized by a rapid but smooth transition from quasi-neutrality in the volume to electron depletion close to the electrodes and chamber walls. The thin non-neutral region, the boundary sheath, comprises only a small fraction of the discharge domain but controls much of its macroscopic behavior. Insights into the properties of the sheath and its relation to the plasma are of high practical and theoretical interest. The recently proposed smooth step model provides a closed analytical expression for the electric field in a planar, radio-frequency modulated sheath. It represents (i) the space charge field in the depletion zone, (ii) the generalized Ohmic and ambipolar field in the quasi-neutral zone, and (iii) a smooth interpolation for the transition in between. This investigation compares the smooth step model with the predictions of a more fundamental particle-in-cell/Monte Carlo collisions simulation and finds good quantitative agreement when the assumed length and time scale requirements are met. A second simulation case illustrates that the model remains applicable even when the assumptions are only marginally fulfilled.

I.   INTRODUCTION

In low pressure radio-frequency (RF) discharges, the electron-depleted sheath occupies only a fraction of the volume but governs many of the phenomena. Its electric field exceeds that of the plasma by three orders of magnitude and plays an important role in the processes of particle acceleration and power absorption. The relation between the sheath charge Q and the sheath voltage V controls the discharge impedance. A solid understanding of the sheath is thus of technological value. Research in this field has a long tradition [1–5].

Theoretical models of the sheath dynamics can be devised in varying degrees of complexity, ranging from lumped element diode models to first-principles numerical simulations [6, 7]. This study addresses the middle ground. Semi-analytic sheath models adopt mathematical simplifications but keep the essential physics. Such models were first analyzed in the 1980s by Godyak et al. [8–10] and Lieberman [11, 12]. Using the fluid approach, they assumed a two-species plasma with electrons and singly charged ions in the RF regime $\omega_{pi} \ll \omega_{RF} \ll \omega_{pe}$. (Here, ω_{RF} is the RF frequency, while ω_{pi} and ω_{pe} are the plasma frequencies of the ions and the electrons, respectively.) Many studies adopted these assumptions [13–22].

The general structure of such sheath models is shown in Fig. 1. As the RF regime is adopted, the model can be separated in two sectors, one that is phase-resolved and one that is not. The phase-resolved sector contains the electron model and Poisson's equation which solve for the electron density $n_e(x,t)$ and the electric field $E(x,t)$. The phase-averaged field $\bar{E}(x)$ reports to the non-phase-resolved sector, where the ion model solves for the ion density $n_i(x)$. This quantity, in turn, is communicated to the phase-resolved sector. Various quantities must be provided as external input, most notably the RF modulation, the flux density of the ions, and the composition, pressure, and temperature of the neutral gas.

RF sheath models are mathematically complicated, and drastic simplifications are called for. Godyak and Lieberman found such a simplification [8–12]. Noting that the transition from electron depletion to quasineutrality in a plasma-sheath transition is steep, they represented the electron density by an infinitely sharp front (hard step) located at the electron edge $s(t)$. This allowed integrating Poisson's equation directly. The resulting hard step model (HSM) provides a closed formula for the electric field $E(x,t)$ in terms of the sheath charge $Q(t)$ and the ion density $n_i(x)$ and simplifies the set-up of sheath models considerably, see Fig. 1. Since then, the HSM has become very popular [13–22].

2
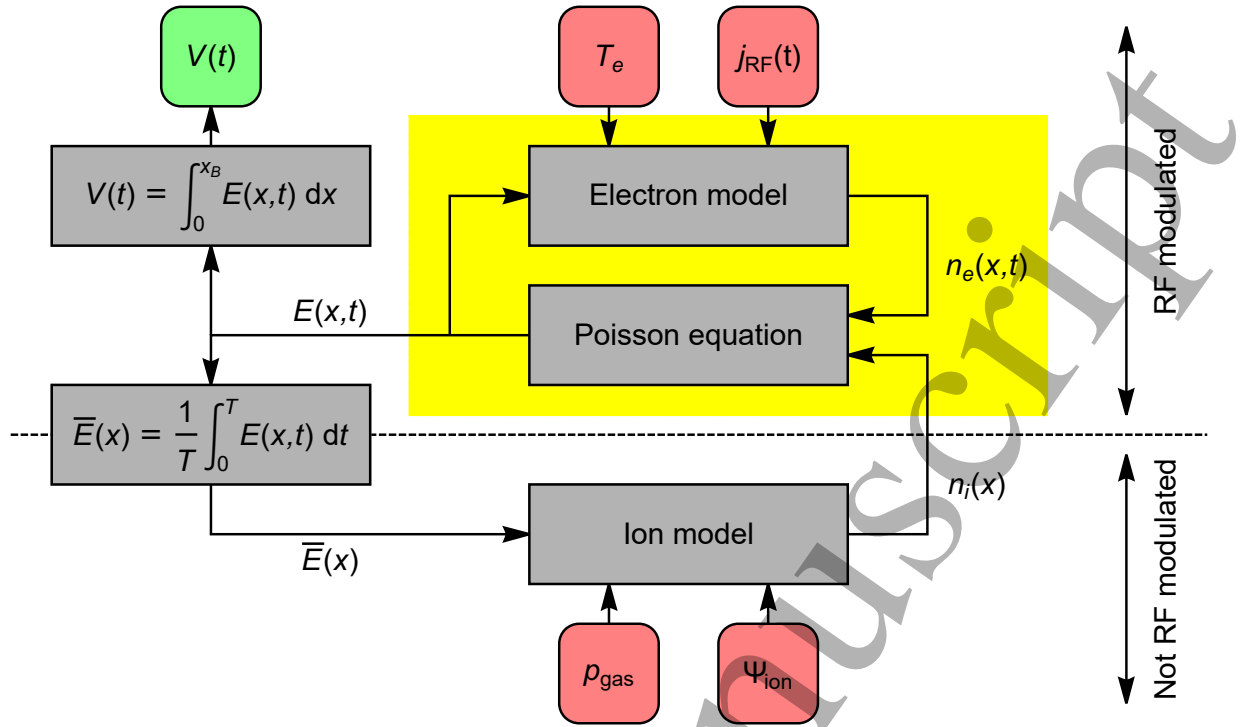
FIG. 1: Structure of an RF boundary sheath model. The RF modulated sector contains the electron model and Poisson's equation which form a system of partial differential equations in x and t. The unmodulated sector contains the ion model, a system of ordinary differential equations in x. The two sectors are coupled via an integral relation which maps the phase-resolved field $E(x,t)$ onto the phase-averaged field $\bar{E}(x)$. Semi-analytic RF boundary sheath models replace the electron and field equations by their approximate solution, i.e., by an effective field model (yellow sector). In the tradition started by Godyak and Lieberman, this effective field model is the HSM [8–22] It is advantageous to substitute it by the SSM [24–27].

However, it is a rather drastic approximation and has, consequently, some severe drawbacks. Implicitly, the HSM sets the electron temperature equal to zero, which renders it impossible to describe the ambipolar field and the floating voltage. Furthermore, it assumes that the electrons can follow the electric field instantaneously; this excludes dynamic phenomena like the action of inertia, the emergence of an Ohmic field, and the effect of field reversal [23].

3

In a recent sequence of studies, one of the current authors proposed an improved formula for the electric field in a sheath-plasma transition, the smooth step model (SSM) [24–26]. This advanced field model accounts for thermal and dynamic effects in terms of a higher-order perturbation analysis. It represents (i) the space charge field in the depletion zone, (ii) the generalized Ohmic and ambipolar field in the quasi-neutral zone, and (iii) a smooth interpolation for the transition in between. The SSM was applied, for example, to set up a consistent theory of electron heating in capacitively coupled plasmas [27].

Nonetheless, the SSM is an approximation based on a fluid model. How does it compare to the outcome of a more fundamental (and more resource-consuming) PIC/MCC-simulation? This is the main question of this study, and we will proceed as follows: In the next section, we sketch the basis of all plasma modeling, kinetic theory, which couples a set of Boltzmann equations for the particle distribution functions to Poisson's equation for the electric field. The PIC/MMC algorithm to solve the kinetic model in a stochastic sense is briefly reviewed. Section III provides a fluid dynamic parent model as the basis of both the HSM and the SSM, and section IV sketches the corresponding derivations. Section V introduces two PIC/MCC simulation cases of a planar capacitively coupled discharge, a single frequency case (1f) and a double frequency case (2f). The cases are evaluated with focus on the sheath dynamics. The electrical field and the sheath voltages predicted by the two models are compared with the results of the PIC/MCC studies. The manuscript concludes with a brief conclusion and an outlook in section VI.

II.   A KINETIC MODEL OF A PLANAR DISCHARGE

Kinetic theory gives the most fundamental model of low temperature gas discharges [28, 29]. We assume a plane-parallel geometry with Cartesian coordinates. The x-axis points from the electrode at the position $x = 0$ to the plasma. The opposite electrode is located at $x = L$. Translational invariance in y and z as well as axisymmetry around the x-axis are assumed. To avoid having to define problematic boundary conditions at the sheath-plasma transition, we treat the whole discharge domain $[0, L]$ and select as the sheath edge x_{B} the first point that is always quasineutral in the RF period. The ion density at the point x_{B} will be called n_{B}. (The slight arbitrariness in these definitions is harmless, as the gradients at x_{B} are small.) The discharge is periodic in the RF period $T_{\mathrm{RF}} = 2\pi/\omega_{\mathrm{RF}}$. Kinetic equations are formulated for the distribution functions $f_s(x, v_\parallel, v_\perp, t)$, $s = 1 \ldots N_{\mathrm{s}}$, where $s = 1 \equiv \mathrm{e}$ refers to electrons and $s \geq 2$ to ions. We use cylindrical velocity coordinates, $v_\parallel \equiv v_x$ and $v_\perp = \sqrt{v_y^2 + v_z^2}$. Moreover, we abbreviate $E \equiv E_x(x, t)$. The term on the right is the collision term to represent elastic and inelastic collisional interaction and chemistry:

$$\frac{\partial f_s}{\partial t} + v_\parallel \frac{\partial f_s}{\partial x} + \frac{q_s}{m_s} E \frac{\partial f_s}{\partial v_\parallel} = \frac{\partial f_s}{\partial t}\Big|_{\mathrm{c}}. \tag{1}$$

At $x = 0$ and $x = L$, boundary conditions are posed. We neglect the emission of secondary particles due to electron or ion impact; instead we assume ideal absorption:

$$f_s(x, v_\parallel, v_\perp, t)|_{x=0} = 0 \ \text{ for } v_\parallel > 0, \tag{2}$$

$$f_s(x, v_\parallel, v_\perp, t)|_{x=L} = 0 \ \text{ for } v_\parallel < 0. \tag{3}$$

We adopt the electrostatic approximation; the electrical field can be expressed by a potential. Poisson's equation applies; the term on the right is the charge density:

$$\varepsilon_0 \frac{\partial E}{\partial x} = -\varepsilon_0 \frac{\partial^2 \Phi}{\partial x^2} = \rho(x, t) = \sum_{s=1}^{N_{\mathrm{s}}} q_s \int_{-\infty}^{\infty} \int_0^{\infty} f_s(x, v_\parallel, v_\perp, t) \, 2\pi \, v_\perp \, \mathrm{d}v_\perp \, \mathrm{d}v_\parallel. \tag{4}$$

The boundary conditions for the potential are as follows, where the RF voltage $V_{\mathrm{RF}}(t)$ is periodic and phase-average free but not necessarily harmonic. We assume floating conditions, i.e., demand that also the discharge current $J(t)$ is phase-average free. The voltage V_{b} is the constant self-bias voltage:

$$\Phi(0, t)|_{x=0} = 0, \tag{5}$$

$$\Phi(L, t)|_{x=L} = V_{\mathrm{b}} + V_{\mathrm{RF}}(t). \tag{6}$$

5

The particle-in-cell/Monte Carlo collisions algorithm provides self-consistent solutions of the kinetic model (1) - (6) in a stochastic sense [30–33]. Its capability to resolve nonlocal and nonlinear effects important for low-pressure plasmas has made it a popular tool [34–39]. We use the benchmarked *yapic1D* [40]. PIC/MCC combines a Lagrangian (particle-based) scheme for the plasma species with an Eulerian (grid-based) calculation of the electric field. In the particle step, an ensemble of superparticles, following the Newton equations of motion, is propagated forward by a small step Δt. This allows to track individual particles and avoids the problem of numerical diffusion. Each superparticle represents w_s physical particles. Masses are scaled $m_s \to w_s m_s$, charges $q_s \to w_s q_s$, densities $n_s \to n_s/w_s$, fluxes $\psi_s \to \psi_s/w_s$, and particle energies $T_s \to w_s T_s$. These scaling laws keep the charge-to-mass ratio q_s/m_s, the thermal speed $\sqrt{T_s/m_s}$ the Debye length λ_{D}, and the plasma frequency ω_{pe} invariant. Individual interactions of particles with the neutral background and the reactor walls are accounted for by Monte Carlo collisions using the null collision method [41]. For the field step, the charges are mapped to a grid of cell size Δx. The calculated fields are interpolated at the particle positions and the cycle starts again, repeated until a periodic state is assumed. Stability and accuracy require the conditions $\Delta t \leq 0.2/\omega_{\mathrm{pe}}$ and $\Delta x \leq 0.5\lambda_{\mathrm{D}}$ to hold [30–33]. Various diagnostics then calculate properties of interest, averaged over a high number of subsequent PIC/MCC cycles for better statistics. Remaining small-scale fluctuations are cleared with the help of a discrete diffusion algorithm; see appendix A for details.

Of particular importance for the interpretation of a discharge simulation are the velocity moments and the corresponding balance equations. All moments are functions of x and t; we list them up to the second order. The moments of order zero are the densities:

$$n_s = \int_{-\infty}^{\infty} \int_0^{\infty} f_s \, 2\pi \, v_\perp \, \mathrm{d}v_\perp \, \mathrm{d}v_\parallel. \tag{7}$$

The first order moments appear as the flux densities ψ_s or mean velocities u_s:

$$\psi_s = n_s u_s = \int_{-\infty}^{\infty} \int_0^{\infty} v_\parallel \, f_s \, 2\pi \, v_\perp \, \mathrm{d}v_\perp \, \mathrm{d}v_\parallel. \tag{8}$$

The moments of order two are the parallel and perpendicular pressures $p_{\parallel s}$ and $p_{\perp s}$ or the parallel and perpendicular temperatures $T_{\parallel s}$ and $T_{\perp s}$, respectively:

$$p_{\parallel s} = n_s T_{\parallel s} = \int_{-\infty}^{\infty} \int_0^{\infty} m_s \left(v_\parallel - u_s\right)^2 f_s \, 2\pi \, v_\perp \, \mathrm{d}v_\perp \, \mathrm{d}v_\parallel, \tag{9}$$

$$p_{\perp s} = n_s T_{\perp s} = \int_{-\infty}^{\infty} \int_0^{\infty} \frac{1}{2} m_s v_\perp^2 f_s \, 2\pi \, v_\perp \, \mathrm{d}v_\perp \, \mathrm{d}v_\parallel. \tag{10}$$

6

Of the balance equations, the first is the particle balance or equation of continuity:

$$\frac{\partial n_s}{\partial t} + \frac{\partial \psi_s}{\partial x} = S_s. \tag{11}$$

The collisional source terms on the right are defined as

$$S_s = \int_{-\infty}^{\infty} \int_0^{\infty} \left.\frac{\partial f_s}{\partial t}\right|_{\mathrm{c}} 2\pi \, v_\perp \, \mathrm{d}v_\perp \, \mathrm{d}v_\parallel. \tag{12}$$

The law of charge conservation is described by

$$\sum_{s=1}^{N_s} q_s S_s = 0. \tag{13}$$

The momentum balances or equations of motion are

$$\frac{\partial}{\partial t}\left(m_s \psi_s\right) + \frac{\partial}{\partial x}\left(m_s \frac{\psi_s \psi_s}{n_s} + n_s T_{\parallel s}\right) = q_s n_s E + \Pi_s. \tag{14}$$

The collision induced changes in the momentum density are:

$$\Pi_s = \int_{-\infty}^{\infty} \int_0^{\infty} m_s v_\parallel \left.\frac{\partial f_s}{\partial t}\right|_{\mathrm{c}} 2\pi \, v_\perp \, \mathrm{d}v_\perp \, \mathrm{d}v_\parallel. \tag{15}$$

In the PIC/MCC simulation, the velocity moments are calculated by summing the respective quantities over all particles in a particular cell.

7

III.   A FLUID PARENT MODEL

As stated in the introduction, the hard step model (HSM) and the smooth step model (SSM) are both based on a fluid approach. This term describes a family of less fundamental plasma theories that involve the first velocity moments of the distribution functions and the corresponding balance equations. The individual fluid theories differ in how many moments are included and how exactly the system of equations is truncated. In this section we describe the leanest fluid model that can serve as a common parent of both the HSM and the SSM. The first step of its derivation is to lump the ion species into a compound fluid,

$$n_{\mathrm{i}} = \frac{1}{e} \sum_{s=2}^{N_{\mathrm{s}}} q_s n_s, \tag{16}$$

$$\psi_{\mathrm{i}} = \frac{1}{e} \sum_{s=2}^{N_{\mathrm{s}}} q_s \psi_s. \tag{17}$$

For the generation rate, the charge conservation law (13) allows to write

$$S_{\mathrm{i}} = \frac{1}{e} \sum_{s=2}^{N_{\mathrm{s}}} q_s S_s = S_{\mathrm{e}} =: S. \tag{18}$$

Then, the electron and ion equations of continuity are

$$\frac{\partial n_{\mathrm{e}}}{\partial t} + \frac{\partial \psi_{\mathrm{e}}}{\partial x} = S, \tag{19}$$

$$\frac{\partial n_{\mathrm{i}}}{\partial t} + \frac{\partial \psi_{\mathrm{i}}}{\partial x} = S, \tag{20}$$

and Poisson's equation reads

$$\varepsilon_0 \frac{\partial E}{\partial x} = e(n_{\mathrm{i}} - n_{\mathrm{e}}). \tag{21}$$

As a result, the total current $J(t)$, the sum of the particle and the displacement currents, is solely a function of time, not position:

$$J(t) = \varepsilon_0 \frac{\partial E}{\partial t} - e\psi_{\mathrm{e}} + e\psi_{\mathrm{i}}. \tag{22}$$

Furthermore, the sheath charge $Q(t)$, defined as the integral of the charge density from the electrode to the bulk point x_{B}, can be expressed as the difference of the electric fields:

$$Q(t) = \int_0^{x_{\mathrm{B}}} e(n_{\mathrm{i}} - n_{\mathrm{e}}) \, \mathrm{d}x = \varepsilon_0 \big(E(x_{\mathrm{B}}, t) - E(0, t) \big). \tag{23}$$

The sheath voltage is the negative integral of the electric field over the sheath:

$$V(t) = - \int_0^{x_{\mathrm{B}}} E(x, t) \, \mathrm{d}x. \tag{24}$$

8

Because of their large mass, the ions solely see the phase-averaged field. Their density is a time-independent function which, as indicated in Fig. 1, can be considered as an input:

$$n_\mathrm{i}(x) = \text{given positive and monotonous function.} \tag{25}$$

It is useful to introduce the so-called charge coordinate $q(x)$,

$$q(x) = \int_0^x e\, n_\mathrm{i}(x')\, \mathrm{d}x'. \tag{26}$$

The ionization term S in the electron continuity equation (19) is negligible in comparison with the other two terms, as the ionization frequency S/n_e is three orders of magnitude smaller than the radio-frequency ω_RF. Furthermore, only the fluctuating (phase-average free) part of the electron flux enters the equation of continuity:

$$\frac{\partial n_\mathrm{e}}{\partial t} + \frac{\partial \tilde{\psi}_\mathrm{e}}{\partial x} = 0. \tag{27}$$

To simplify the electron momentum balance we interpret the interaction of electrons with neutrals as friction and neglect the non-fluctuating part of the electron flux:

$$\frac{\partial}{\partial t}\left(m_\mathrm{e}\tilde{\psi}_\mathrm{e}\right) + \frac{\partial}{\partial x}\left(m_\mathrm{e}\frac{\tilde{\psi}_\mathrm{e}^2}{n_\mathrm{e}} + n_\mathrm{e}T_\mathrm{e}\right) = -en_\mathrm{e}E - \nu_\mathrm{e}m_\mathrm{e}\tilde{\psi}_\mathrm{e}. \tag{28}$$

The electron friction constant is treated as an input:

$$\nu_\mathrm{e} = \text{given positive constant.} \tag{29}$$

Also the electron temperature is treated as an input. Traditionally assumed to be a constant, it may more generally be a function provided by other sectors of the model:

$$T_\mathrm{e}(x,t) = \text{given positive, RF-periodic function.} \tag{30}$$

The floating condition implies that the phase-averaged flux of the electrons $\bar{\psi}_\mathrm{e}$ and of the ions $\bar{\psi}_\mathrm{i}$ must be equal at the electrode. As $\bar{\psi}_\mathrm{e}$ has already been dropped from the model, the Hertz-Langmuir relation is employed to restore it [13]:

$$\left|\bar{\psi}_\mathrm{e}\right|\big|_{x=0} = \sqrt{\frac{T_\mathrm{e}}{2\pi m_\mathrm{e}}}\,\bar{n}_\mathrm{e}\big|_{x=0} \overset{!}{=} \left|\psi_\mathrm{i}\right|\big|_{x=0} = \text{given constant.} \tag{31}$$

Taking the time derivative of (23), invoking (22) and (31), and neglecting the fluctuating components of the electron flux at $x = 0$ and the displacement current at x_B, we get

$$\frac{\mathrm{d}Q}{\mathrm{d}t} = -J(t). \tag{32}$$

The RF current $J(t)$ is treated as an input:

$$J(t) = \text{given RF periodic, phase-average free function.} \tag{33}$$

9

IV. HARD STEP MODEL AND SMOOTH STEP MODEL

As discussed, semi-analytical sheath models require a closed formula to express the electric field in the sheath-to-plasma transition in terms of the ion density and the sheath charge. The HSM and the SSM provide such closed formulas. They start from the same assumptions regarding the spatial and temporal scales, here formulated in the terminology of [26]:

- The transition from electron depletion to quasi-neutrality occurs within a thin zone. The governing scale of this transition is the Debye length λ_D, while the sheath extension scales with the gradient lengths l of the ion density and the electron temperature T_e. The corresponding smallness parameter is termed ϵ:

$$\epsilon = \frac{\lambda_D}{l} = \sqrt{\frac{\varepsilon_0 T_e}{e^2 n_i}} \frac{1}{n_i} \frac{\partial n_i}{\partial x} \sim \sqrt{\frac{\varepsilon_0 T_e}{e^2 n_i}} \frac{1}{T_e} \frac{\partial T_e}{\partial x} \ll 1. \tag{34}$$

- The RF modulation frequency ω_{RF} is small compared to the plasma frequency ω_{pe}. Thus, the electrons behave quasi-statically. The electron collision frequency ν_e and the modulation rate of the electron temperature T_e are assumed to be comparable to ω_{RF}. The corresponding smallness parameter is termed η:

$$\eta = \frac{\omega_{RF}}{\omega_{pe}} = \frac{\omega_{RF}}{\sqrt{e^2 n_i / \varepsilon_0 m_e}} \ll 1. \tag{35}$$

The HSM implements these assumptions in a drastic way; the smallness parameters ϵ and η are both set equal to zero. Equivalently, one can simply set the electron temperature T_e and the electron mass m_e equal to zero. The equation of motion (28) then reduces to $n_e E = 0$. To solve this equation, the ansatz of a hard step in the electron density is made:

$$n_{e,HSM}(x,t) = \begin{cases} 0 & : \ x < s(t) \\ n_i(x) & : \ x > s(t) \end{cases}. \tag{36}$$

Equation (32) is time-integrated under the condition that the minimal value of $Q(t)$ is zero; this corresponds to the asymptotic form of the Hertz-Langmuir relation (31) under the assumptions of the HSM. The location of the hard step $s(t)$, with a minimum that is also zero, is determined by the sheath charge $Q(t)$ via

$$Q(t) = \int_0^{s(t)} e n_i(x') \, dx', \tag{37}$$

10

Integrating Poisson's equation (21), one can express the electric field of the HSM as follows. In the unipolar region, the field reflects the charge between $s(t)$ and x. In the ambipolar zone, it is, due to $T_e \to 0$ and $m_e \to 0$, identical to zero. The space charge field is accounted for, but thermal and dynamical effects are completely neglected:

$$E_{\mathrm{HSM}}(x,t) = \frac{1}{\varepsilon_0} \min\left(q(x) - Q(t), 0\right) = \begin{cases} -\dfrac{e}{\varepsilon_0} \displaystyle\int_x^s n_i(x')\, dx' & : x < s(t) \\ 0 & : x > s(t) \end{cases}. \quad (38)$$

The SSM treats the parent model equations more cautiously. An asymptotic series in ϵ and η is formulated and truncated after the quadratic order ([26] offers a more detailed description). In physical units, the electrical field provided by the SSM reads

$$E_{\mathrm{SSM}}(x,t) = -\sqrt{\frac{n_i T_e}{\varepsilon_0}} \Xi_S\left(\frac{q(x) - Q(t)}{\sqrt{\varepsilon_0 n_i T_e}}\right) - \frac{1}{e n_i} \frac{\partial}{\partial x}(n_i T_e) \Xi_A\left(\frac{q(x) - Q(t)}{\sqrt{\varepsilon_0 n_i T_e}}\right) \quad (39)$$
$$+ \frac{m_e}{e^2 n_i}\left(\frac{\partial J}{\partial t} + \nu_e J - \frac{1}{e}\frac{\partial}{\partial x}\left(\frac{J^2}{n_i}\right)\right)\Xi_\Omega\left(\frac{q(x) - Q(t)}{\sqrt{\varepsilon_0 n_i T_e}}\right).$$

The sheath charge $Q(t)$ is obtained by solving (32) under the Hertz-Langmuir relation (31). The special functions Ξ_S, Ξ_A, and Ξ_Ω (displayed in [26]) are smooth – in fact analytical – functions of their argument ξ. By defining the formal electron edge $s(t)$ via equation (37), one can interpret ξ as a scaled distance of the position x to that point [24]:

$$\xi = \frac{q(x) - Q(t)}{\sqrt{\epsilon_0 n_i T_e}} \approx \frac{x - s(t)}{\lambda_D}. \quad (40)$$

The SSM is a representation of the electric field which accounts for thermal and dynamic effects in leading order perturbation theory:

- In the unipolar region left of the transition, $q(x) \ll Q(t)$. The function Ξ_S becomes equal to its negative argument, while Ξ_A and Ξ_Ω vanish. The resulting form describes, asymptotically exact, the space charge field and coincides with the HSM:

$$E_S(x,t) = \frac{q(x) - Q(t)}{\varepsilon_0}. \quad (41)$$

- In the ambipolar region right of the transition, $q(x) \gg Q(t)$, the function Ξ_S vanishes, while Ξ_A and Ξ_Ω become unity. The field reduces to what is known as the generalized Ohmic field including the ambipolar field [42]:

$$E_{A\Omega}(x,t) = -\frac{1}{e n_i}\frac{\partial}{\partial x}(n_i T_e) + \frac{m_e}{e^2 n_i}\left(\frac{\partial J}{\partial t} + \nu_e J - \frac{1}{e}\frac{\partial}{\partial x}\left(\frac{J^2}{n_i}\right)\right). \quad (42)$$

- In the transition zone, formula (39) provides a smooth transition from (41) to (42).

11

V.   COMPARISON OF SSM AND PIC/MCC

We now provide a comparison of the SSM and a PIC/MCC simulation for two selected cases, a single-frequency case (1f) at a frequency $f_{RF} = 13.56\,MHz$ and a double-frequency case (2f) with $f_{RF1} = 13.56\,MHz$ and $f_{RF2} = 4 \times f_{RF1} = 54.24\,MHz$. The electrode gap is $L = 50\,mm$. The discharge gas is argon at $T_g = 300\,K$; the gas density is calculated from the ideal gas law. The simulation traces the trajectories of electrons ($s = e \equiv 1$) and Ar^+ ions ($s = i \equiv 2$). The chemistry of the electrons includes elastic scattering, an effective excitation collision, and the ionization process. The Ar^+ ion processes are elastic scattering and charge exchange collisions with the parent gas. All cross sections are drawn from the Phelps database [43–47]. The sticking factor of all particles was assumed as unity, secondary emission was neglected. Table I provides some more details on the chemistry set.

No.	reaction	process name	threshold energy
1	$e + Ar \rightarrow e + Ar$	elastic scattering	-
2	$e + Ar \rightarrow e + Ar^*$	effective excitation	$11.5\,eV$
3	$e + Ar \rightarrow e + Ar^+ + e$	ionization	$15.8\,eV$
4	$Ar^+ + Ar \rightarrow Ar^+ + Ar$	elastic scattering	-
5	$Ar^+ + Ar \rightarrow Ar + Ar^+$	charge exchange collisions	-

TABLE I: Collision processes considered in the PIC/MCC simulation. The cross sections for the electrons are from Yamabe et al. [44], the cross sections for the ions are from Phelps [43]. The database is distributed via the LXCat project [45–47]. A graphical representation of the data is found in previous work [48].

Case (1f) was intensively studied as the "base case" of a tutorial on plasma simulation [36], case (2f) has a different excitation and a lower pressure. Both cases were run with a high count of superparticles per species ($N_{SP,1f} \approx 300.000$, $N_{SP,2f} \approx 160.000$) to assure reliability. Furthermore, the results of the converged states were averaged over 100.000 RF-cycles each. In combination with the smoothing and regularization algorithm described in the appendix, a satisfactory noise reduction was achieved. All sheath quantities discussed in the following refer to the sheath at the left electrode $x = 0$. The point x_B was placed $3\,mm$ right of the maximum value of the formal electron sheath edge $s(t)$.

12

A. Single frequency case (1f)

Case (1f) is driven by $V_{\mathrm{RF}}(t) = V_0 \sin(\omega_{\mathrm{RF}} t)$, where $V_0 = 500\,\mathrm{V}$ and $\omega_{\mathrm{RF}} = 2\pi \times 13.56\,\mathrm{MHz}$. The pressure is $p = 3\,\mathrm{Pa}$. The domain is split into $M = 1000$ intervals of $\Delta x = 5 \times 10^{-5}\,\mathrm{mm}$; the RF period into $N = 4000$ steps of $\Delta t = 1.84 \times 10^{-11}\,\mathrm{s}$.
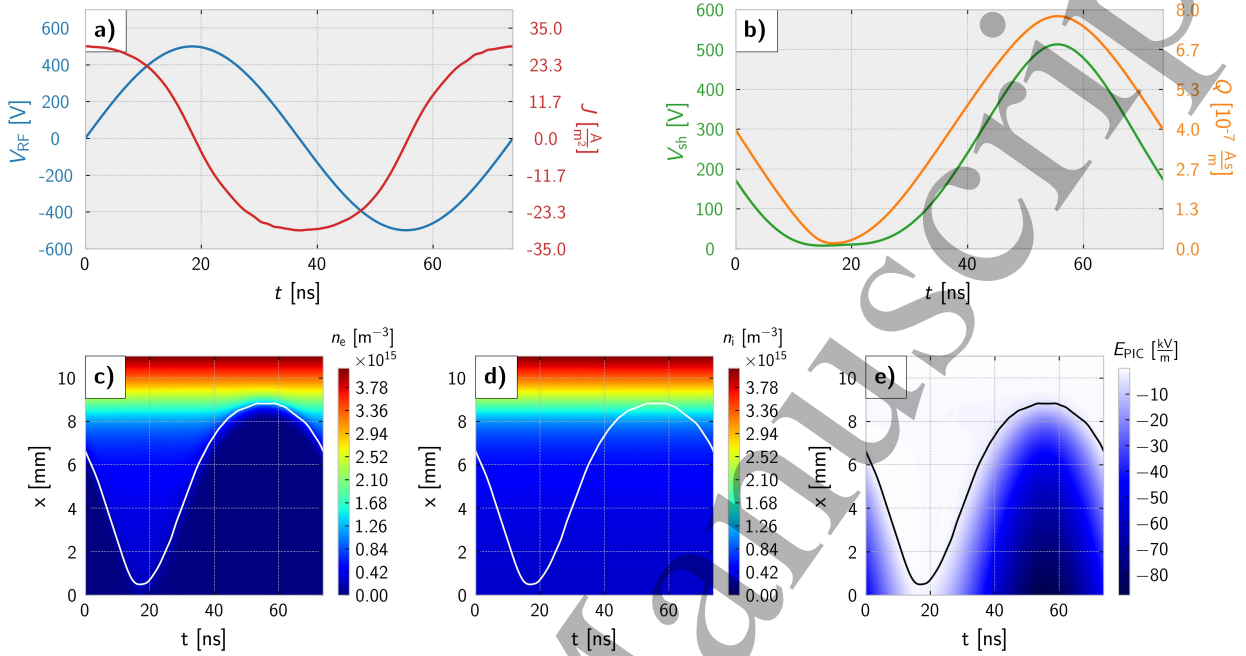

FIG. 2: Simulation results for the case 1f. a) RF voltage V_{RF} (blue) and discharge current J (red). b) sheath voltage V_{sh} (green) and sheath charge Q (orange). c) to e): spatially and temporally resolved profiles of the electron density n_{e}, the ion density n_{i}, and the electric field strength E_{PIC}. The white (in c), d)) and black (in e)) lines mark the position of the formal electron edge $s(t)$. Conditions: $V_0 = 500\,\mathrm{V}$, $\omega_{\mathrm{RF}} = 2\pi \times 13.56\,\mathrm{MHz}$, $L = 50\,\mathrm{mm}$, $p = 3\,\mathrm{Pa}$.

Fig. 2 a) shows the applied voltage and the resulting, nearly harmonic current density $J(t)$ which has a phase shift to the applied voltage of about 88°. Fig. 2 b) shows the sheath charge $Q(t)$ and the sheath voltage $V_{\mathrm{sh}}(t)$. The sheath charge $Q(t)$ is obtained by evaluating the right-hand side of equation (23), the sheath voltage represents the integrated field (24). Fig. 2 c) and d) show the particle densities in the sheath interval $[0, x_{\mathrm{B}}]$, with $x_{\mathrm{B}} = 11\,\mathrm{mm}$. The ion density is stationary; the electrons are modulated. Fig. 2 e) displays the electric field. It is strong in the electron depleted zone $x < s(t)$ but weak in the ambipolar zone $x > s(t)$. The formal electron edge $s(t)$ is marked in the lower panels of Fig. 2 by white or black lines. It is related to the sheath charge $Q(t)$ by the relation $q(s(t)) = Q(t)$.
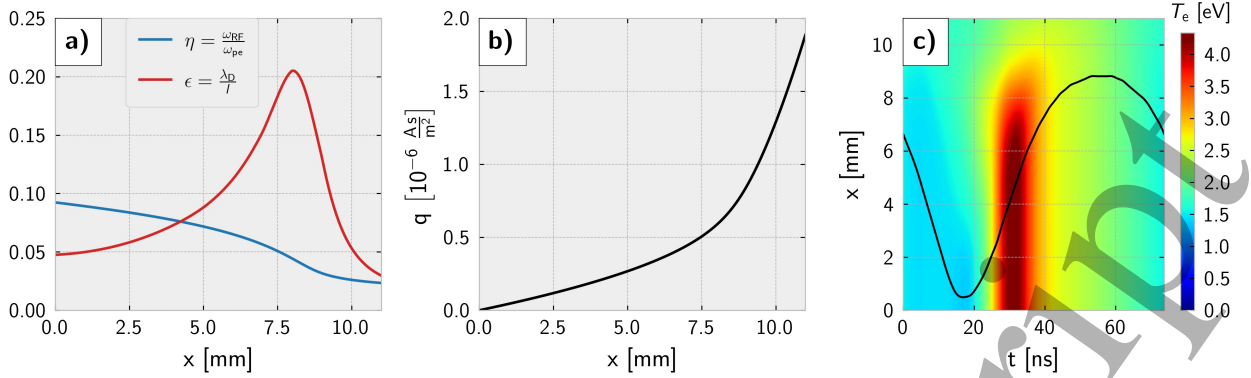
13

FIG. 3: Input for the SSM as provided by the PIC/MCC case (1f). a) Smallness parameters η and ϵ as function of position x. b) Charge coordinate function $q(x)$. c) Spatio-temporally resolved profile of the regularized electron temperature $T_e(x,t)$. The black line marks the formal electron edge $s(t)$. Conditions: $V_0 = 500\,\mathrm{V}$, $\omega_{\mathrm{RF}} = 2\pi \times 13.56\,\mathrm{MHz}$, $L = 50\,\mathrm{mm}$, $p = 3\,\mathrm{Pa}$.

Fig. 3 a) shows the smallness parameters ϵ and η as a function of x, evaluated for time-averaged values of n_i and T_e. The frequency ratio $\eta = \omega_{\mathrm{RF}}/\omega_{\mathrm{pe}}$ (blue) is below 0.1 which indicates quasi-static behavior. The length scale ratio $\epsilon = \lambda_D/l$ (red) reaches a maximum of 0.2. Altogether, the SSM should be a valid approximation. Fig. 3 b) gives the function $q(x)$, Fig. 3 c) the regularized temperature $T_{\|e}(x,t)$ which fills the role of T_e (see appendix).

Fig. 4 a) to c) show the temporally and spatially resolved profiles of the electric fields $E(x,t)$. The HSM Fig. 4 a) represents the space charge field correctly, but the ambipolar and Ohmic fields in the quasi-neutral zone are missing, as shown in Fig. 4 d) with $\Delta E_{\mathrm{HSM}} = E_{\mathrm{HSM}} - E_{\mathrm{PIC}}$. In contrast, the SSM covers both the space charge field and the ambipolar and Ohmic fields. This gives a much lower error; Fig. 4 e) gives $\Delta E_{\mathrm{SSM}} = E_{\mathrm{SSM}} - E_{\mathrm{PIC}}$. Figs. 4 f) to l) depict the electric field of the HSM, the SSM and the PIC/MCC simulation as a function of time for selected positions within the sheath. A blue background indicates that a point (x,t) is in the depletion region $x < s(t)$, a gray background that it is in the ambipolar region $x > s(t)$. Again, in the unipolar zone, the HSM and the SSM are both exact. In the ambipolar zone, the HSM gives a zero field, while the SSM represents the PIC/MCC data quite reasonably, with a relative error below $10\,\%$. The remaining deviations originate from different sources. The fluid model which underlies the SSM has a limited accuracy, it cannot resolve the non-local aspects of the dynamics. Additionally, there are errors due to the approximation itself, the static error at the maximum of $\epsilon(x)$ at $x \approx 8\,\mathrm{mm}$ and the dynamic error around $s(t)$.
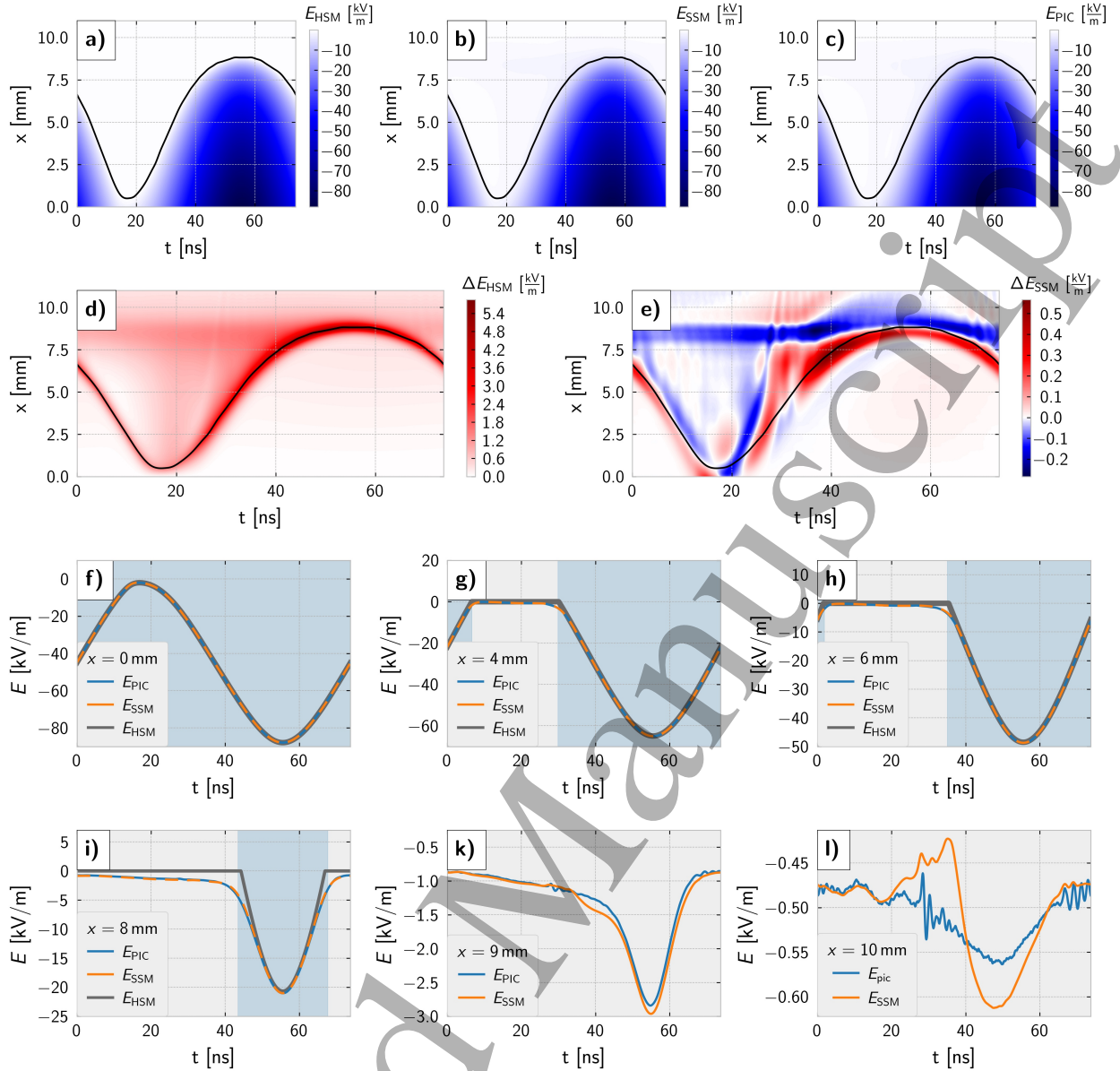
14

FIG. 4: Comparison of the electric field of case (1f) as calculated by HSM, SSM, and PIC/MCC. First row: spatio-temporal profile of the electric field given by a) HSM, b) SSM, c) PIC/MCC. Second row: profiles of the differences d) $\Delta E_{\mathrm{HSM}} = E_{\mathrm{HSM}} - E_{\mathrm{PIC}}$, and e) $\Delta E_{\mathrm{SSM}} = E_{\mathrm{SSM}} - E_{\mathrm{PIC}}$. The black curves denote the position of the formal electron edge $s(t)$. Third and fourth row: temporally resolved profiles of the electric field at selected locations displaying the differences of the HSM, SSM and PIC/MCC fields in detail. (In panels k) and l), the HSM field is equal to zero.) Blue background marks the unipolar zone $x < s(t)$, white background the ambipolar zone $x > s(t)$. Conditions: $V_0 = 500\,\mathrm{V}$, $\omega_{\mathrm{RF}} = 2\pi \times 13.56\,\mathrm{MHz}$, $L = 50\,\mathrm{mm}$, $p = 3\,\mathrm{Pa}$.
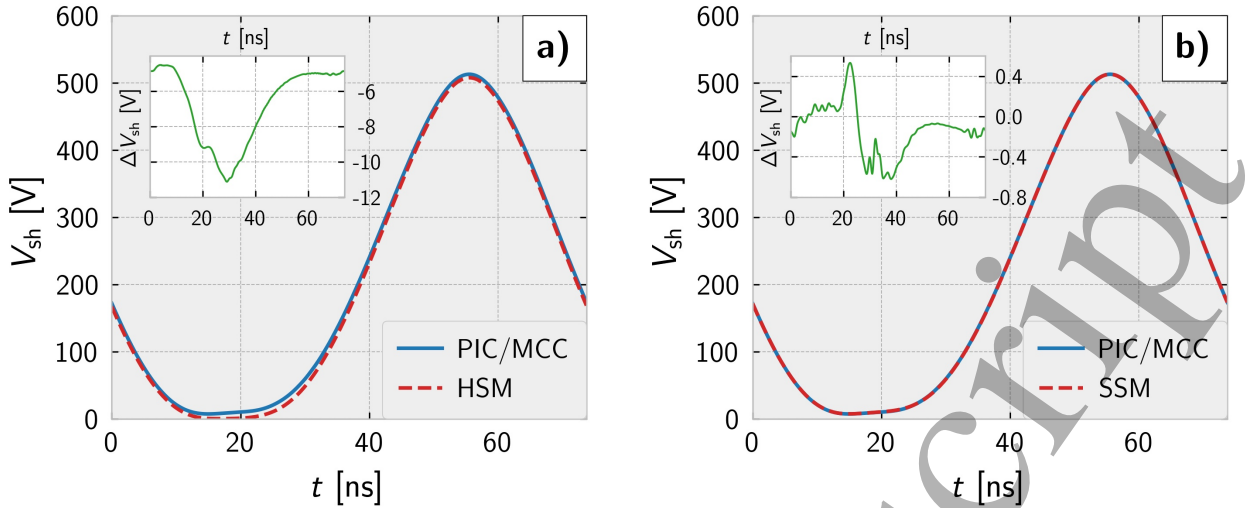
FIG. 5: Comparison of the model sheath voltages V_{sh} to the simulation data for the case (1f). a): comparison for the HSM. The inset shows the error $\Delta V_{\mathrm{sh}} = V_{\mathrm{sh,HSM}} - V_{\mathrm{sh,PIC}}$. b): comparison for the SSM. The inset shows the error $\Delta V_{\mathrm{sh}} = V_{\mathrm{sh,SSM}} - V_{\mathrm{sh,PIC}}$. Conditions: $V_0 = 500\,\mathrm{V}$, $\omega_{\mathrm{RF}} = 2\pi \times 13.56\,\mathrm{MHz}$, $L = 50\,\mathrm{mm}$, $p = 3\,\mathrm{Pa}$.

Integrated quantities have an even smaller error. Fig. 5 shows a comparison of the predicted sheath voltages of a) HSM and b) the SSM to the simulation data. Already the HSM gives a solid approximation of the sheath voltage V_{sh} with an error in the range of a few percent. It misses, however, the physically important contribution of the ambipolar and Ohmic fields. The SSM corrects that error, and the resulting curves cannot be distinguished (Fig. 5 b)). The inset demonstrates that the difference is indeed very small. The relative error of the total sheath voltage swing is less than one percent.

16

B.　Dual frequency case (2f)

Case 2f describes a dual-frequency discharge driven by $V_{\mathrm{RF}}(t) = V_1 \sin(\omega_{\mathrm{RF1}} t) + V_2 \sin(\omega_{\mathrm{RF2}} t)$, where $V_1 = V_2 = 200\,\mathrm{V}$, $\omega_{\mathrm{RF1}} = 2\pi \times 13.56\,\mathrm{MHz}$, and $\omega_{\mathrm{RF2}} = 2\pi \times 54.24\,\mathrm{MHz}$, see Fig. 6 a). The pressure is $p = 1\,\mathrm{Pa}$. The domain is split into $M = 800$ intervals of $\Delta x = 6.25 \times 10^{-5}\,\mathrm{mm}$, the RF period into $N = 2200$ steps of $\Delta t = 3.35 \times 10^{-11}\,\mathrm{s}$. The case is chosen to lie at the edge of the validity domain of the SSM.
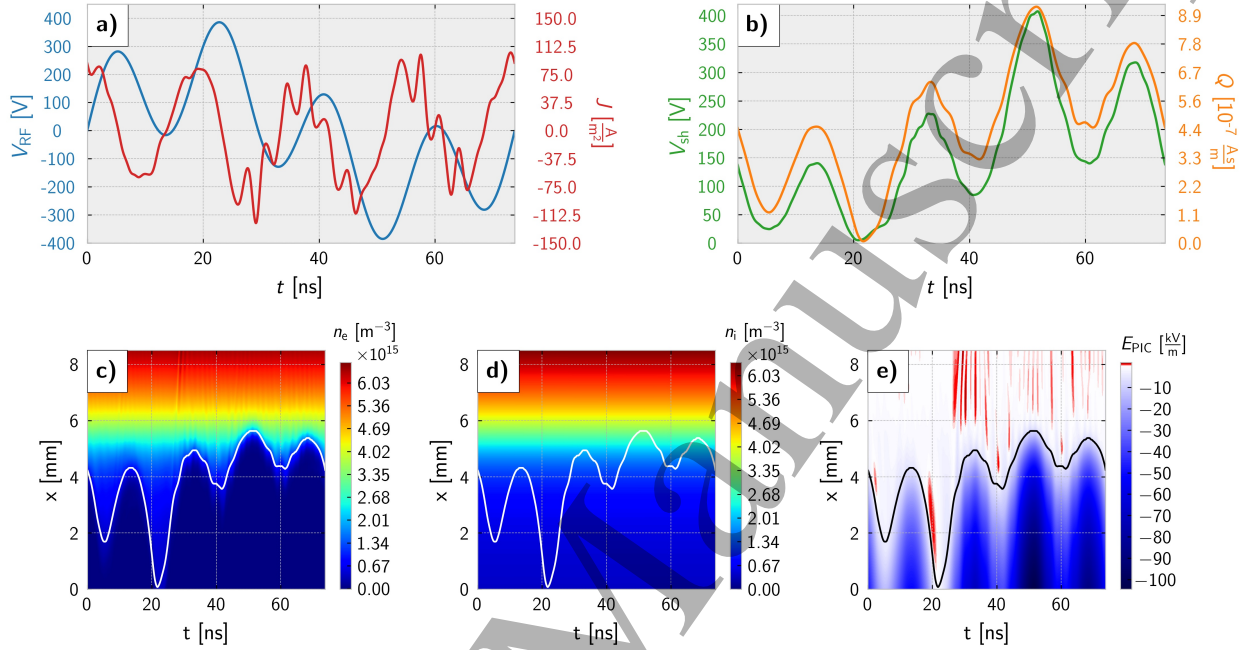

FIG. 6: Simulation results for the case 2f. a) RF voltage V_{RF} (blue) and discharge current J (red). b) sheath voltage V_{sh} (green) and sheath charge Q (orange). c) to e): spatially and temporally resolved profiles of c) the electron density n_{e}, d) the ion density n_{i}, and e) the electric field E_{PIC}. The white (c), d)) and black (e)) lines denote the position of the formal electron edge $s(t)$. $V_1 = V_2 = 200\,\mathrm{V}$, $\omega_{\mathrm{RF1}} = 2\pi \times 13.56\,\mathrm{MHz}$, $\omega_{\mathrm{RF2}} = 2\pi \times 54.24\,\mathrm{MHz}$, $L = 50\,\mathrm{mm}$, $p = 1\,\mathrm{Pa}$.

Fig. 6 a) shows the discharge current $J(t)$ which differs strongly from the current of case (1f). In addition to modes in the externally applied frequencies, it shows self-excited oscillations at higher frequencies which are the hallmark of the plasma series resonance (PSR) [49]. The corresponding sheath charge $Q(t)$ and sheath voltage $V_{\mathrm{sh}}(t)$ are displayed in Fig. 6 b). Figs. 6 c), d), and e) show the densities and the field in the interval $[0, x_{\mathrm{B}}]$, with $x_{\mathrm{B}} = 8\,\mathrm{mm}$. While the ion density is stationary, the electron density and the field are strongly modulated and show fast electrostatic plasma oscillations in the ambipolar zone [50].

17

Fig. 7 a) depicts the spatial distribution of the parameters ϵ and η. The length scale ratio ϵ behaves comparable to the case (1f) and just displays the expected maximum at $x \approx 4.5\,\mathrm{mm}$. The frequency ratio η, however, is much larger; quasi-static behavior may not be present. Fig. 7 shows also the function $q(x)$ and the regularized parallel temperature $T_{\parallel\mathrm{e}}(x,t)$.
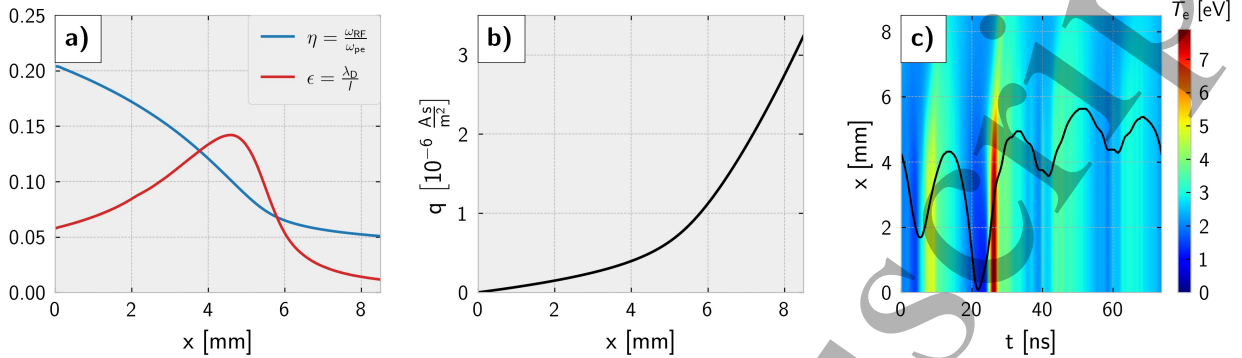

FIG. 7: Parameters for the SSM formula calculated from the PIC/MCC simulation of the case 2f. a) smallness parameters η and ϵ a function of position x. b) the charge coordinate function $q(x)$. c) the spatially and temporally resolved profile of the regularized electron temperature T_{e}. The black line marks the position of the formal electron edge $s(t)$. Conditions: $V_1 = V_2 = 200\,\mathrm{V}$, $\omega_{\mathrm{RF1}} = 2\pi \times 13.56\,\mathrm{MHz}$, $\omega_{\mathrm{RF2}} = 2\pi \times 54.24\,\mathrm{MHz}$, $L = 50\,\mathrm{mm}$, $p = 1\,\mathrm{Pa}$.

Figs. 8 a) to c) depict temporally and spatially resolved profiles of the electric field $E(x,t)$, Figs. 8 d) and e) show the deviations $\Delta E_{\mathrm{HSM}} = E_{\mathrm{HSM}} - E_{\mathrm{PIC}}$ and $\Delta E_{\mathrm{SSM}} = E_{\mathrm{SSM}} - E_{\mathrm{PIC}}$, and Figs. 8 f) to l) present temporal profiles at selected locations. Again, a blue background marks momentarily unipolar points (x,t), a gray background momentarily ambipolar ones. As in the (1f) case, both models cover the depletion field and are exact in the unipolar zone. Likewise, the HSM continues to fail in the ambipolar zone, giving a vanishing electric field. Now, however, also the SSM has difficulties there. It is not capable to reproduce the rapid electrostatic oscillations of the PIC/MCC field on the scale of the plasma frequency ω_{pe}. Instead, due to its quasistatic character, it resorts to some kind of temporal average value. The corresponding error is largest immediately after the sheath collapse when the excitation of the resonances is strongest [20, 21, 49]. One can also detect the static error connected to the maximum in the length scale ratio ϵ, although it is overshadowed by the rapid oscillations. Despite these noticable shortcomings, the SSM provides a significantly better approximation of the effective electric field in the considered regime than the HSM.
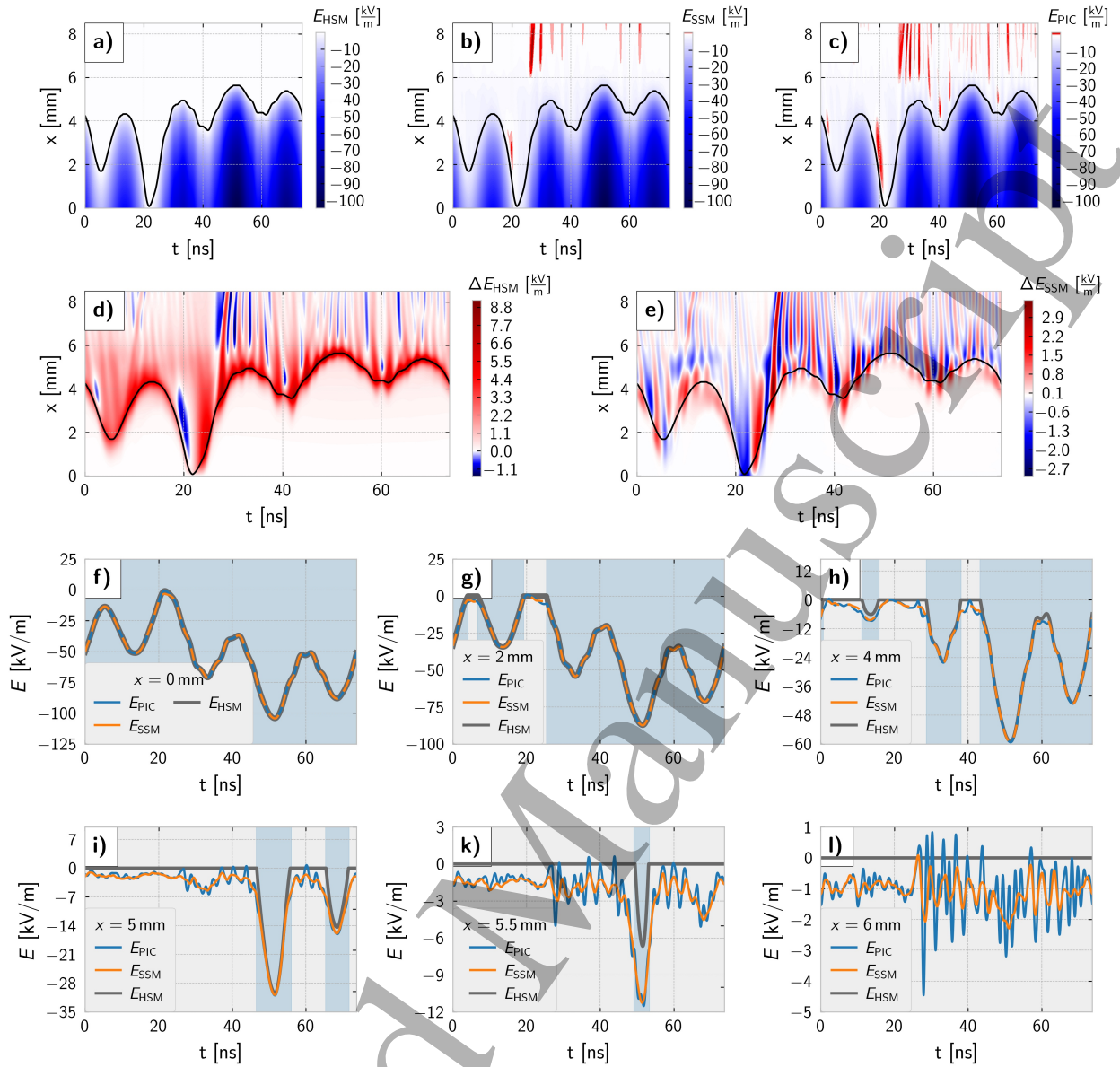
18

FIG. 8: Comparison of the electric field of case (2f) as calculated by HSM, SSM, and PIC/MCC. First row: spatio-temporal profile of the electric field given by a) HSM, b) SSM, c) PIC/MCC. Second row: profiles of the differences d) $\Delta E_{\mathrm{HSM}} = E_{\mathrm{HSM}} - E_{\mathrm{PIC}}$, and e) $\Delta E_{\mathrm{SSM}} = E_{\mathrm{SSM}} - E_{\mathrm{PIC}}$. The black curves denote the position of the formal electron edge $s(t)$. Third and fourth row: temporally resolved profiles of the electric field at selected locations displaying the differences of the HSM, SSM and PIC/MCC fields in detail. Blue background marks the unipolar zone $x < s(t)$, white background the ambipolar zone $x > s(t)$. Conditions: $V_1 = V_2 = 200\,\mathrm{V}$, $\omega_{\mathrm{RF1}} = 2\pi \times 13.56\,\mathrm{MHz}$, $\omega_{\mathrm{RF2}} = 2\pi \times 54.24\,\mathrm{MHz}$, $L = 50\,\mathrm{mm}$, $p = 1\,\mathrm{Pa}$.
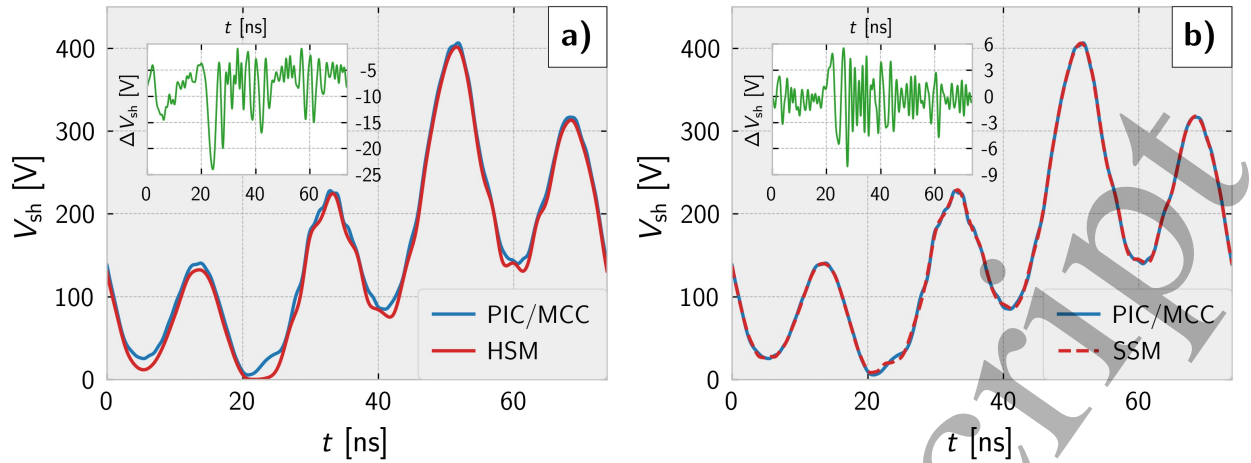
19

FIG. 9: Comparison of the model sheath voltages V_{sh} with the PIC/MCC simulation for case (2f). a) HSM, inset giving $\Delta V_{\mathrm{sh}} = V_{\mathrm{sh,HSM}} - V_{\mathrm{sh,PIC}}$. b) SSM, inset giving $\Delta V_{\mathrm{sh}} = V_{\mathrm{sh,SSM}} - V_{\mathrm{sh,PIC}}$. Conditions: $V_1 = V_2 = 200\,\mathrm{V}$, $\omega_{\mathrm{RF1}} = 2\pi \times 13.56\,\mathrm{MHz}$, $\omega_{\mathrm{RF2}} = 2\pi \times 54.24\,\mathrm{MHz}$, $L = 50\,\mathrm{mm}$, $p = 1\,\mathrm{Pa}$.

Fig. 9 shows a comparison of the sheath voltages V_{sh} predicted by the HSM (Fig. 9 a)) and the SSM (Fig. 9 b)) to that of the PIC/MCC simulation. For the HSM, the differences are evident and the inset shows that the sheath voltage is severely underestimated for this case. The largest error appears when the voltage has a minimum and can be close to 100 percent. In contrast, the prediction of the SSM is still quite reliable, even though the underlying assumptions are only marginally met. The voltage curves in Fig. 9 b) are virtually identical; the total error does not exceed a few percent. The inset shows that the difference is almost average-free and fluctuates with high frequency. This results from the presence of electrostatic oscillations in the ambipolar region which are not resolved by the SSM.

20

VI. CONCLUSION AND OUTLOOK

The smooth step model (SSM) is an approximate solution of the electron equations of motion and Poissons's equation in the RF regime $\omega_{\mathrm{pi}} \ll \omega_{\mathrm{RF}} \ll \omega_{\mathrm{pe}}$. The subject of this manuscript is the validation of the SSM, using simulations with a particle-in-cell/Monte Carlo collisions (PIC/MCC) code as reference. Comparisons are also made with the hard step model (HSM). Two exemplary discharge configurations were chosen. Both employ the same capacitively coupled parallel plate reactor with a gap width of $L = 50\,\mathrm{mm}$. The single frequency case (1f) operates with $\omega_{\mathrm{RF}} = 2\pi \times 13.56\,\mathrm{MHz}$ at a pressure of $p = 3\,\mathrm{Pa}$; the dual frequency case (2f) runs with $\omega_{\mathrm{RF1}} = 2\pi \times 13.56\,\mathrm{MHz}$, $\omega_{\mathrm{RF2}} = 2\pi \times 54.24\,\mathrm{MHz}$, $p = 1\,\mathrm{Pa}$. To make the comparison as meaningful as possible, the noise of the PIC/MCC field was reduced by smoothing.

The SSM performs as expected: In the (1f) case, where the prior assumptions are well met, the deviations from the PIC/MCC standard are small. The electric field is captured well, phase-resolved and phase-averaged. In the unipolar zone, the SSM is asymptotically exact, a feature shared with the HSM. In the ambipolar region, it gives a reliable approximation. The small deviation from the PIC/MCC comparison field arises from a number of sources: First, there are the errors caused by the mathematical approximation technique itself, i.e., the use of a truncated asymptotic series in the small parameters $\eta = \omega_{\mathrm{RF}}/\omega_{\mathrm{pe}}$ and $\epsilon = \lambda_{\mathrm{D}}/l$. This can be seen, for example, in the static error related to the maximum of the parameter ϵ. Then, there may be an error inherited from the underlying fluid model: The description of the collisional momentum loss by a friction ansatz is limited, especially at low-pressure [52]. Still, the SSM outperforms the HSM which neglects Ohmic and ambipolar fields altogether. The sheath voltage as a spatially integrated quantity has an error of less than $1\,\%$.

The situation is different in the case (2f). Here, the smallness parameter η reaches 20%, which indicates that the assumption of a quasi-static behavior is only marginally fulfilled. And indeed, high-frequent oscillations on the scale of the plasma frequency ω_{pe} are observed in the ambipolar zone, most strongly excited at the moment of the sheath collapse [20, 21, 49]. The SSM is, by its quasistatic nature, not able to follow these fast electrostatic oscillations and results in a temporally averaged field. (Again, the SSM performs better than the HSM which predicts a vanishing electric field.) The overall sheath voltage is still captured well. This is a general trend; spatially integrated quantities are generally less influenced by local (i.e., spatially small-scale) structures.

21

In sum, we state that the validation of the SSM was successful. The approximation is valid in the regime it was designed for, namely in the RF regime where $\omega_{\rm pi} \ll \omega_{\rm RF} \ll \omega_{\rm pe}$ and $\lambda_{\rm D} \ll l$. (Actually, only the condition $\omega_{\rm RF} \ll \omega_{\rm pe}$ may be critical; $\lambda_{\rm D} \ll l$ is self-fulfilling as the ion density gradient length l scales with $\lambda_{\rm D}$ itself. Work is in progress to relax $\omega_{\rm pi} \ll \omega_{\rm RF}$.) Compared to the HSM, the SSM is superior. This statement is less about quantitative accuracy than physical fidelity. What is missing in the HSM are, in the words of Bohm [5], "...the small plasma fields [which], compared with sheath fields, are so small that they produce negligible changes of potential over distances many sheath thicknesses in extent. [...] However, the plasma fields cannot be completely neglected, because over the long distances that they cover they are able to accelerate positive ions up to appreciable energies, of the order of the plasma electron temperature." (Lieberman, in his 1988 analytical solution for the capacitive RF sheath which employed the HSM, solved that problem by postulating the Bohm criterion at the sheath edge [11].) Moreover, these plasma field are also responsible for the processes of plasma heating. The HSM, which expresses the sheath voltage $V_{\rm sh}$ as an exact function of the sheath charge Q and the sheath current as its derivative, $j = {\rm d}Q/{\rm d}t$, leads to a vanishing value for the RF averaged power deposition, $\bar{P} = \oint V(Q)\,{\rm d}Q/T = 0$ [35]. The SSM, in contrast, delivers a more physical result [27]. We are posititive that the SSM will find also other uses in the modeling of RF driven gas discharges, for example for the definition of effective boundary sheath models [51].

Acknowledgement

ORCID IDs:

M. Klich: https://orcid.org/0000-0002-3913-1783

S. Wilczek: https://orcid.org/0000-0003-0583-4613

T. Mussenbrock: http://orcid.org/0000-0001-6445-4990

R.P. Brinkmann: https://orcid.org/0000-0002-2581-9894

REFERENCES

[1] C.D. Child, *Phys. Rev.* **32**, 492 (1911)

[2] I. Langmuir, *Phys. Rev. (Series II)*, **2**, 450 (1913)

[3] N.F. Mott. R.W. Gurney, *Electronic Processes in Ionic Crystals*, Clarendon, Oxford (1940)

[4] R. Warren, *Phys. Rev.* **98**, 1658 (1955)

[5] D. Bohm, A. Guthry and R.K. Wakerling eds., *The Characteristics of Electrical Discharges in Magnetic Fields*, McGraw-Hill, New York (1949)

[6] A. Metze, D.W. Ernie, H.J. Oskam, *J. Appl. Phys.* **60**, 3081 (1986)

[7] M. Shihab, D. Ziegler, R.P. Brinkmann, J. Phys. D: Appl. Phys. **45**, 185202 (2012)

[8] V.A. Godyak and Z.K. Ghanna, *Sov. J. Plasma Phys.* **6**, 372 (1979)

[9] V.A: Godyak, *Soviet radio frequency discharge research*, Falls Church, VA: Delphic Associates (1986).

[10] V.A. Godyak and N. Sternberg, *Phys. Rev. A* **42**, 2299 (1990)

[11] M.A. Lieberman, *IEEE Trans. Plasma Sci.* **16**, 638 (1988)

[12] M.A. Lieberman, *IEEE Trans. Plasma Sci.* **17**, 338 (1989)

[13] K.U. Riemann, *J. Appl. Phys.* **65**, 999 (1989)

[14] P.M. Vallinga, P.M Meijer, F.J. de Hoog, *J. Phys. D: Appl. Phys.* **22**, 1650 (1989)

[15] N. Sternberg, V.A. Godyak, *J. Comp. Phys.*, **111**, 347 (1994)

[16] H.C. Kim, J.K. Lee, J.W. Shon *Phys. Plasmas* **10**, 4545 (2003)

[17] K. Börnig *Appl. Phys. Lett.* **60**, 1553 (1992)

[18] M.A. Sobolewski, *Phys. Rev. E* **62**, 8540 (2000)

[19] E. Kawamura, V. Vahedi, M.A. Lieberman1, C.K. Birdsall, *Plasma Sources Sci. Technol.* **8**, R45 (1999)

[20] T. Mussenbrock, D. Ziegler, R.P. Brinkmann, *Phys.. Plasmas* **13**, 083501 (2006).

[21] D. Ziegler, T. Mussenbrock, R.P. Brinkmann, *Plasma Sources Sci. Technol.* **17**, 045011 (2008).

[22] U. Czarnetzki, Phys. Rev. E Stat. Nonlin. Soft Matter Phys. **88**, 063101 (2013)

[23] J. Schulze, Z. Donko, B.G. Heil, D. Luggenhölscher, T Mussenbrock, R.P. Brinkmann, U. Czarnetzki, *J. Phys. D: Appl. Phys* **41**, 105214 (2008)

[24] R.P. Brinkmann, *J. Appl. Phys.* **102**, 093303 (2007)

[25] R.P. Brinkmann, *J. Phys. D: Appl. Phys.* **44**, 042002 (2011)

[26] R.P. Brinkmann, Plasma Sources Sci. Technol. **24**, 064002 (2015)

[27] R.P. Brinkmann, Plasma Sources Sci. Technol. **25**, 014001 (2016)

[28] M.A. Lieberman, A.J. Lichtenberg, "Principles of Plasma Discharges and Materials Processing", Wiley, New York (2005)

[29] T. Makabe, Z. Petrovic, *Plasma Electronics: Applications in Microelectronic Device Fabrication*, CRC Press, Boca Raton (2015)

[30] C. K. Birdsall, IEEE Trans. on Plasma Sci. **19** 65 (1991)

[31] D. Vender and R.W. Boswell, J. Vac. Sci. Technol. A **10**, 1331 (1992).

[32] J.P. Verboncoeur Plasma Phys. Control. Fusion **47** A231–A260 (2005)

[33] D. Tskhakaya, K. Matyash, R. Schneider, F. Taccogna, Contrib. Plasma Phys. **47**, 563 (2007)

[34] S. Wilczek, J. Trieschmann, D. Eremin, R.P. Brinkmann, J. Schulze, E. Schuengel, A. Derzsi, I. Korolov, P. Hartmann, Z. Donkó, T. Mussenbrock, Phys. Plasmas **23**, 063514 (2016)

[35] J. Schulze, Z. Donkó, T. Lafleur, S. Wilczek, R.P. Brinkmann, Plasma Sources Sci. Technol. **27**, 055010 (2018)

[36] S. Wilczek, J. Schulze, R.P. Brinkmann, Z. Donkó, J. Trieschmann, T. Mussenbrock, J. Appl. Phys. **127**, 181101 (2020)

[37] B. Horváth, J. Schulze, Z. Donkó, and A. Derzsi, J. Phys. D: Appl. Phys. **51**, 355204 (2018)

[38] A. Derzsi, B. Horváth, I. Korolov, Z. Donkó, and J. Schulze, J. Appl. Phys. **126**, 043303 (2019)

[39] Z. Donkó, Plasma Sources Sci. Technol. **20**, 024001 (2011)

24

[40] M.M. Turner, A. Derzsi, Z. Donkó, D. Eremin, S. J. Kelly, T. Lafleur, and T. Mussenbrock, Physics of Plasmas **20**, 013507 (2013)

[41] H.R. Skullerud *J. Phys. D: Appl. Phys.* **1**, 1567 (1968)

[42] "The Generalized Ohm's Law in Plasma". In: Plasma Astrophysics. Astrophysics and Space Science Library, **341**, Springer, New York, NY (2006)

[43] A. V. Phelps, J. Appl. Phys. **76**, 747 (1994)

[44] C. Yamabe, S. J. Buckman and A. V. Phelps, Phys. Rev. A **27**, 1345 (1983)

[45] S. Pancheshnyi, S. Biagi, M. Bordage, G. Hagelaar, W. Morgan, A. Phelps, and L. Pitchford, Chem. Phys. **398**, 148–153 (2012)

[46] L. Alves, Journal of Physics: Conference Series, **565**, 012007 (2014)

[47] L. C. Pitchford, L. L. Alves, K. Bartschat, S. F. Biagi, M.-C. Bordage, I. Bray, C. E. Brion, M. J. Brunger, L. Campbell, A. Chachereau et al. Plasma Processes Polym. **14**, 1600098 (2017)

[48] M. Klich, S. Wilczek, J. F. J. Janssen, R. P. Brinkmann, T. Mussenbrock and J. Trieschmann, Plasma Sources Sci. Technol. **30** 065019 (2021)

[49] U. Czarnetzki, T. Mussenbrock, R.P. Brinkmann Phys. Plasmas **13**, 123503 (2006)

[50] Oscillations in ionized gases L. Tonks, I. Langmuir, Phys. Rev. **33**, 195 (1929)

[51] T. Samir, S. Wilczek, M. Klich, T. Mussenbrock, R.P. Brinkmann, *APS Gaseous Electronics Conference*, LT2.006 (2020)

[52] M. Vass, S. Wilczek, T. Lafleur, R.P. Brinkmann, Z. Donko, J. Schulze, *Plasma Sources Sci. Technol.* **30**, 065015 (2021).

25

Appendix A: Details on the smoothing and regularization schemes

The SSM requires the ion density profile $n_i(x)$, the electron temperature profile $T_e(x, t)$, and the temporal wave forms of the RF current $J(t)$ and the sheath charge $Q(t)$ as input. For validation purposes, these input quantities are here taken from PIC-MCC simulations. PIC-MCC data are typically quite noisy, which is amplified when derivatives are taken. Therefore, a suitable smoothing process is imperative. This is all the more true as our work analyzes differences between simulation results and a fairly reliable analytical approximation. We assume that all output data are organized as spatial vectors with elements $1 \dots M$, as temporal vectors with elements $1 \dots N$, or as spatio-temporal matrices of size $M \times N$. Linear smoothing is achieved by multiplying all spatially discretized numerical data (vectors) with a diffusion matrix D_x, and all temporally discretized data with a diffusion matrix D_t. In both instances, the diffusion matrices are constructed as the matrix exponential of the discretized second order derivative operator (stencil). The implementations differ slightly due to differing boundary conditions:

- Assuming homogeneous Neumann conditions, the matrix representation of the second order spatial derivative (stencil) reads as follows. Note that the matrix is symmetric. The smallest eigenvalue is $\lambda_0 = 0$; it corresponds to the eigenvector $(1, 1, 1 \dots, 1, 1, 1)^T$. All other eigenvalues λ_m are positive

$$\nabla_x^2 = \begin{pmatrix} -1 & 1 & 0 & \dots & 0 & 0 & 0 \\ 1 & -2 & 1 & \dots & 0 & 0 & 0 \\ 0 & 1 & -2 & \dots & 0 & 0 & 0 \\ \dots & \dots & \dots & \dots & \dots & \dots & \dots \\ 0 & 0 & 0 & \dots & -2 & 1 & 0 \\ 0 & 0 & 0 & \dots & 1 & -2 & 1 \\ 0 & 0 & 0 & \dots & 0 & 1 & -1 \end{pmatrix} \tag{A1}$$

  The spatial diffusion matrix D_x is then realized as follows, where $\exp(\cdot)$ denotes the matrix exponential and Δ controls the half-width of the resulting diffusion kernel. The highest eigenvalue is unity, all other eigenvalues are smaller but positive:

$$D_x(s) = \exp\left(-\frac{1}{2}\Delta^2\nabla^2\right). \tag{A2}$$

26

- Assuming periodic boundary conditions, the matrix representation of the second order temporal derivative (stencil) reads as follows. Again, the matrix is symmetric. The smallest eigenvalue is $\lambda_0 = 0$; it corresponds to the eigenvector $(1, 1, 1 \ldots, 1, 1, 1)^T$. All other eigenvalues λ_n are positive

$$\nabla_t^2 = \begin{pmatrix} -2 & 1 & 0 & \ldots & 0 & 0 & 1 \\ 1 & -2 & 1 & \ldots & 0 & 0 & 0 \\ 0 & 1 & -2 & \ldots & 0 & 0 & 0 \\ \ldots & \ldots & \ldots & \ldots & \ldots & \ldots & \ldots \\ 0 & 0 & 0 & \ldots & -2 & 1 & 0 \\ 0 & 0 & 0 & \ldots & 1 & -2 & 1 \\ 1 & 0 & 0 & \ldots & 0 & 1 & -2 \end{pmatrix} \tag{A3}$$

The diffusion matrix is then realized as

$$D_t = \exp\left(-\Delta^2 \nabla_t^2\right) \tag{A4}$$

After some experimentation, we decided that a value of $\Delta = 10$ delivers the right balance between under- and over-smoothing: It eliminates much of the noise, but keeps the physical features intact and introduces no noticeable artifacts. We are currently working on a strict criterion to determine the optimal value of Δ. Several other smoothing methods were tried, for instance least-square fitting of cubical splines, but did not prove superior.

In addition, the temperature data $T_{\parallel e}$ and $T_{\perp e}$ require regularization. This arises from their definition as the ratio of the electron pressure to the electron density, equations (9) and (10). Where the electrons are depleted, the quantities are irregular. Regularization is achieved by replacing the ill-defined points in the sheath by their last reliable contemporary counterparts at the bulk-sheath transition. This procedure is applied when the electron density falls below a value of 20% of the ion density. One can infer from formula (39), that details of the regularization scheme are not critical, due to the nature of the special SSM functions [26]: In the depletion zone $q \ll Q$, the field assumes the limit form (41) which is independent of T_e. A previous work [36] discusses the original data of Fig. 3 c).

27